

## Full length article

## Highly sensitive fiber force sensor based on cascaded Fabry-Perot cavities and Vernier effect

Hongyu Fu<sup>a</sup>, Sisu Peng<sup>a</sup>, Pengcheng Li<sup>a</sup>, Chuanxin Teng<sup>b</sup>, Christophe Caucheteur<sup>c</sup>, Hang Qu<sup>a,\*</sup>, Xuehao Hu<sup>c,\*</sup><sup>a</sup> Research Center for Advanced Optics and Photoelectrics, Department of Physics, College of Science, Shantou University, Shantou, Guangdong 515063, China<sup>b</sup> Guangxi Key Laboratory of Optoelectronic Information Processing, Guilin University of Electronic Technology, Guilin 541004, China<sup>c</sup> Department of Electromagnetism and Telecommunication, University of Mons, Boulevard Dolez 31, Mons 7000, Belgium

## ARTICLE INFO

## Keywords:

F-P cavity

Force sensor

UV-curable adhesive

Vernier effect

## ABSTRACT

In this article, we introduce a new concept for an in-line optical fiber force sensor probe, which is based on two cascaded Fabry-Perot (F-P) cavities to generate the Vernier effect and enhance sensitivity. Due to the significantly low Young's modulus of UV-cured adhesive within the sensing cavity, extremely high force sensitivity is obtained. In our initial sample, we achieved an impressive force sensitivity of  $-61,301 \text{ nm/N}$ . To improve that, the optical path difference between the two cavities is further reduced, exhibiting a remarkable increased force sensitivity of  $-140,813 \text{ nm/N}$ . As an application, we conducted an experiment using this highly sensitive force sensor probe to measure the evaporation rate of ethanol, a common solvent, which is  $7.79 \times 10^{-5} \text{ g/s}$  at room temperature. The proposed sensor features advantages of high sensitivity, simple structure, ease of fabrication, compactness, which is an ideal fiber sensor probe for sensitive force measurement.

## 1. Introduction

For the past two decades, optical fiber sensors have been playing very important role in different fields, such as medical, pharmaceutical, environmental, biosensing and food industries. Plenty of applications have been carried out to detect a variety of parameters, like humidity [1,2] strain and force [3,4], refractive index [5,6], temperature [7,8], magnetic field intensity [9,10] and curvature [11,12]. For the measurement of force, different sensing mechanisms have been involved, such as Fiber-optic Sagnac sensors [13], Fabry-Perot (F-P) interferometric sensors [14], and grating-based sensors (both fiber Bragg gratings and long period fiber gratings [15]). Among these sensing configurations, the Fabry-Perot interferometric sensor plays an important role due to its simple structure, ease of fabrication, and relatively high sensitivity.

For example, Wei *et al.* produced a flexible force sensor based on spheroidal F-P air cavity obtained by splicing two core-etched single-mode fibers (SMFs) with a sensitivity up to  $106 \text{ pm/N}$  in the range of  $0\text{--}20 \text{ N}$  [16]. Arata *et al.* introduced an ultra-miniature F-P pressure/force sensor at the end of an optical fiber. The length of the cavity between the fiber end and a diaphragm was adjustable by pressure. Then, the element was encapsulated inside a carbide pin showing a force

sensitivity of  $2.52 \text{ nm/N}$  with a range of  $\pm 25 \text{ N}$  [17]. Liu *et al.* proposed a force sensor based on fiber F-P micro-cavity and plugged by cantilever taper. The force sensitivity was measured to  $841.59 \text{ nm/N}$  in the range from  $0$  to  $0.4 \text{ N}$  thanks to the ultra-long active-length of capillary and the ultra-short interference length of the air cavity [18].

Recently, two-photon-polymerization (TPP)-based 3D printing technique has been utilized to fabricate F-P fiber sensor probes for force measurements down to the scale of piconewtons. By printing a micro-spring on a fiber facet, a force sensitivity of  $0.436 \text{ nm/nN}$  and a resolution of  $40.0 \text{ pN}$  were obtained [19]. Additionally, a microcantilever printed on a fiber facet shows an ultra-high force sensitivity of  $154 \text{ nm/}\mu\text{N}$  and a force resolution of up to  $130 \text{ pN}$  [20]. Though significantly force sensitivity improvement has been achieved, the high precision 3D printing system typically utilize expensive femtosecond laser system, and the printing process is rather sophisticated and time-consuming.

Although F-P fiber interferometers have shown relatively high sensitivity for force measurements, they could be further upgraded by combining other configurations, such as Vernier effect, which is more and more attractive for sensing applications [21,22]. This effect results from the spectral overlap of two cascaded interferometers with slightly detuned free spectral ranges (FSRs) or interference frequencies.

\* Corresponding authors.

E-mail addresses: [haqux@stu.edu.cn](mailto:haqux@stu.edu.cn) (H. Qu), [xuehao.hu@umons.ac.be](mailto:xuehao.hu@umons.ac.be) (X. Hu).<https://doi.org/10.1016/j.optlastec.2024.110825>

Received 13 December 2023; Received in revised form 14 February 2024; Accepted 6 March 2024

Available online 10 March 2024

0030-3992/© 2024 Elsevier Ltd. All rights reserved.

Generally, one of the interferometers works as a reference unit, while the other one acts as a sensing unit [23]. The output signal of the configuration with Vernier effect is the overlay of the two interferometric spectra with periodic envelopes, called “beats” [24]. The force perturbation from the sensing cavity could induce dramatic shifts of the envelopes of the spectra, significantly amplifying the sensitivity of the sensors [25].

Zhao *et al.* proposed a sensor with two F-P interferometers to generate the Vernier effect. The reference interferometer was formed by a section of hollow tube sandwiched between two SMFs. The other sensing interferometer was modified by inserting a tapered FBG in the hollow tube, not only maintaining the similar cavity length, but also enhancing the strain sensitivity. The strain sensitivity of the proposed sensor reached 1.307 nm/ $\mu\epsilon$  [26]. However, the fabrication process of the sensing cavity remains complex with the tapered fiber. Bao *et al.* proposed two fiber F-P interferometers with mirrors micromachined by the slit fs-laser beam. The reference interferometer was composed of the silica fiber, while the sensing interferometer relied on hyperelastic polydimethylsiloxane (PDMS) fiber. Due to Vernier effect, the proposed sensor had a force sensitivity of 45.721 nm/ $\mu\text{N}$  in the range from 0 to 1400  $\mu\text{N}$  [27]. Though very high force sensitivity was achieved, the fabrication of the PDMS fiber and fs-laser-induced mirrors were time-consuming.

In fiber-optic sensing field, polymer materials, especially photopolymerizable resins have been widely utilized as a bridge between two SMFs, as they present advantages as compared with silica material due to its lower Young's modulus, higher elastic, etc. For example, Oliveira *et al.* demonstrated a hydrostatic pressure F-P sensor with polymerized resin between two SMFs acting as a cavity [28]. Lee *et al.* proposed a fiber sensor to measure tilt angles. The sensing structure was based on a tapered polymer between two SMFs [29].

Motivated by the properties of Vernier effect and polymer adhesives, we combine both advantages and propose two in-line fiber-optic sensor probes based on two cascaded F-P cavities for force measurement. The UV-curable adhesive in the sensing cavity plays an important role due to its small Young's modulus. Two sensor probes with different cavity parameters present different performances. For Sample 1, a force sensitivity of  $-61,301$  nm/N was obtained. For Sample 2, an ultra-high sensitivity of  $-140,813$  nm/N was obtained due to the further reduction of the optical path difference between the two cavities. As a proof-of-principle application, we demonstrate to use of the sensor to measure the evaporation rate of ethanol. As compared to the regular F-P fiber sensor fabricated by sandwiching UV adhesive between two SMF pig-tails, the sensitivity of the proposed sensor is improved by  $\sim 62$  folds. Additionally, although some fiber force probes fabricated by TPP-based 3D printing of ultrafine structures on fiber feature sensitivities as high as  $10^8$  nm/N. Note that fabrication of these probes is technically challenging and expensive, as fs-lasers and high-precision motion manipulation systems are normally involved. Moreover, these ultra-fine structures have relatively low mechanical strength and tend to break down due to mis-operation. The sensor probes proposed in this paper have the advantages of simple structure, quite low cost, simple manufacturing process, commercial availability of required materials and high sensitivity. The proposed sensor could be used in the fields where precise force detection is relevant.

## 2. Principle of F-P cavity and Vernier effect

### 2.1. Principle of F-P cavity and effect

The working principle of the proposed fiber sensor is first based on F-P interferometer fiber sensor with a single cavity, whose FSR is expressed by Refs. [30,31]:

$$FSR = \frac{\lambda^2}{2nL} \quad (1)$$

where  $\lambda$ ,  $n$  and  $L$  represent the wavelength of light in vacuum, the refractive index inside the cavity and the cavity length, respectively. Then, a second cavity is cascaded to generate the Vernier effect, which significantly amplifies the sensitivity of the F-P interferometer fiber sensor. The FSR of the envelope can be written as [32,33]:

$$FSR_e = \frac{FSR_1 \times FSR_2}{|FSR_1 - FSR_2|} \quad (2)$$

The sensitivity amplification factor is expressed as [34]:

$$M = \frac{FSR_e}{FSR_1} = \frac{FSR_2}{|FSR_1 - FSR_2|} = \frac{n_1 L_1}{|n_1 L_1 - n_2 L_2|} \quad (3)$$

where  $FSR_1$ ,  $FSR_2$  represent the FSR for interference spectra of Cavity<sub>1</sub> and Cavity<sub>2</sub>, and  $FSR_e$  represent the FSR of the spectral envelope in the reflection spectrum of the whole sensor probe. If the FSR of the envelope is large or the two cavities have similar optical length (OL), the sensitivity of the cascaded F-P fiber sensor can be dramatically improved.

### 2.2. Sensor probe fabrication

The structure of the proposed sensor is illustrated in Fig. 1. An SMF pigtail (SMF<sub>1</sub>) and a short segment of SMF (SMF<sub>2</sub>) are spliced by UV glue. For the ease of handling, SMF<sub>2</sub> is also fusion-spliced with a segment of capillary fiber which acts as a mechanical support. The UV glue between SMF<sub>1</sub> and SMF<sub>2</sub> forms the resonant Cavity<sub>1</sub> with a length  $L_1$ , SMF<sub>2</sub> forms the resonant Cavity<sub>2</sub> with a length  $L_2, and Cavity<sub>1</sub> and Cavity<sub>2</sub> together form combined Cavity<sub>3</sub>. The interface between SMF<sub>1</sub> and the UV glue constitutes Mirror<sub>1</sub>; the interface between the UV glue and SMF<sub>2</sub> constitutes Mirror<sub>2</sub>; and the interface between SMF<sub>2</sub> and the air inside the capillary forms Mirror<sub>3</sub>. In this case, three F-P cavities are obtained. Cavity<sub>1</sub> is composed of the UV glue of which the optical length is very sensitive to force. Cavity<sub>2</sub> is composed of the SMF<sub>2</sub>. Thus, Cavity<sub>3</sub> is a combination of Cavity<sub>1</sub> and Cavity<sub>2</sub> with a cavity length of  $L_1 + L_2$ . The schematic of the sensor probe is depicted in Fig. 1.$

The sensor probe used in this work was fabricated based on the following steps. Firstly, an SMF was spliced with a silica capillary fiber (Polymicro Technologies, TSP075150, inner diameter: 75  $\mu\text{m}$ , outer diameter: 124  $\mu\text{m}$ .) using a fusion splicer (Fujikura, FSM-100P). During the discharge process, the electric electrodes were not positioned at the interface between the capillary and the SMF, but mostly on the SMF side by using the manual mode of the fusion splicer to avoid the collapse or deformation of the capillary. Then, the SMF was cleaved into the designated length,  $L_2$  for Cavity<sub>2</sub> using a fiber cleaver with the aid of a long working-distance microscope. The cleaved SMF-capillary segment and another SMF pigtail were then aligned with a gap using a three-axis micro-positioning stage (Thorlabs, MBT616D/M). Length of the gap could be approximately adjusted into the proper length,  $L_1$ , for Cavity<sub>1</sub> with the aid of the optical microscope as well. After that, UV-curable adhesive (Norland, NOA 73) was filled in the gap between the two

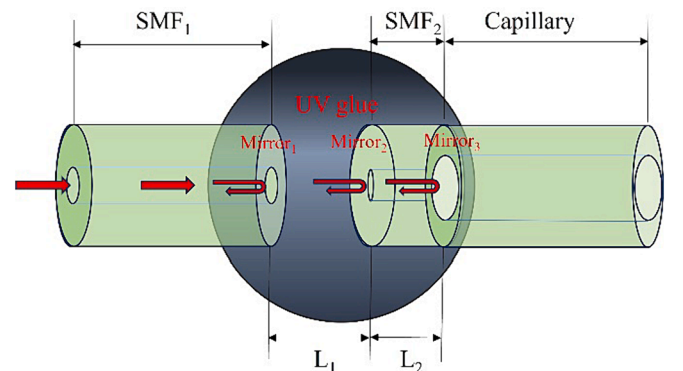


Fig. 1. Sketch of the cascaded Fabry-Perot cavity fiber sensor.

SMFs, and the gap was further finely adjusted to obtain an appropriate spectrum envelope by monitoring the reflected spectrum. Finally, the adhesive was cured for  $\sim 30$  s using a UV lamp (SJMAEA, wavelength: 365 nm) with an illumination intensity of  $12 \text{ mW/cm}^2$ . The adhesive features a Young's modulus of 0.011 GPa, and a tensile strength of 0.0014 GPa. More information about this adhesive could be found on the official website [35]. The Young's modulus of the silica-based SMF is 69.2 GPa [36]. The optical microscopic images of the two samples are shown in the insets of Fig. 2.

Prior to the force measurement, the sensor probes were annealed at  $60^\circ\text{C}$  for 5 h to increase the strength and stability of the UV adhesive. For force measurements, the sensor probes were vertically placed. At the bottom of this sensor, the capillary fiber was connected to a carrier platform made of paper using four lightweight threads. During the measurement, the weight was gradually added to the carrier platform, and the force is subsequently calculated by  $F = mg$ , where  $m$  and  $g$  represent the weight and gravity acceleration ( $g \approx 10 \text{ m/s}^2$ ), respectively. The spectrum of the sensor was recorded after each addition of weight. The reflection spectrum demodulation system includes a broadband light source (BBS) (YSL Photonics, SC-5-FC), a fiber circulator and an optical spectrum analyzer (Anritsu, MS9740A). Since the bandwidth of the envelope is wide, fitting methods, such as Gaussian fitting and Lorentz fitting, are necessary to apply to improve the accuracy of the peak wavelength reading. In this work, the position of the envelope is determined by the central wavelength of the peak calculated by Lorentz fitting. All the force measurements were conducted in a temperature-controlled environment.

### 3. Experimental and numerical results

#### 3.1. The first sample

For Sample 1,  $L_1$  and  $L_2$  are set to be  $\sim 120 \text{ }\mu\text{m}$  and  $\sim 130 \text{ }\mu\text{m}$ , respectively. The  $FSR_e$  of the resulting spectrum is  $\sim 220 \text{ nm}$ . Reflection spectra were measured in the range from 1300 nm to 1700 nm. With increasing external force ranging from 0 to  $28.8 \times 10^{-4} \text{ N}$ , the spectral envelope exhibits blue-shifts, as shown in Fig. 3. Using Lorentzian fitting on each spectrum, the peak wavelength of the envelope was precisely shifted from the initial position at 1534.8 nm–1365.8 nm. This experiment was conducted for three times, exhibiting good repeatability. Via linear fitting, the force sensitivity of  $-61,301 \text{ nm/N}$  was obtained, as shown in Fig. 4.

Using the above structural parameters ( $L_1 = 119.2 \text{ }\mu\text{m}$ ,  $L_2 = 130.3 \text{ }\mu\text{m}$ ), the reflection spectra under different forces can be calculated numerically using the theoretical equations presented in Ref. [31]. For Cavity<sub>1</sub>, the Young's modulus is 0.011 GPa, while the counterpart for

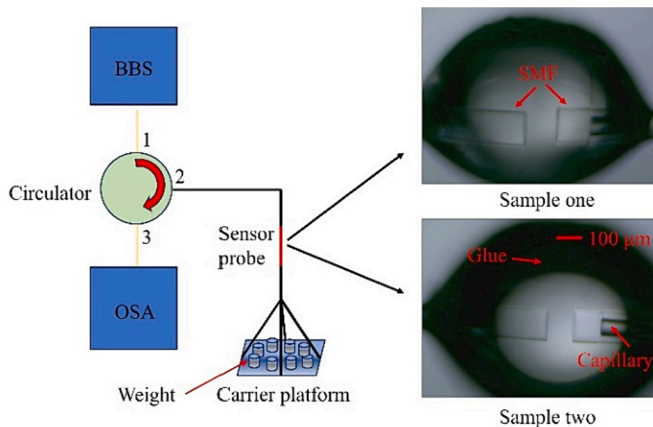


Fig. 2. Device setup diagram for force measurements. The insets are microscopic images of the sensor probes.

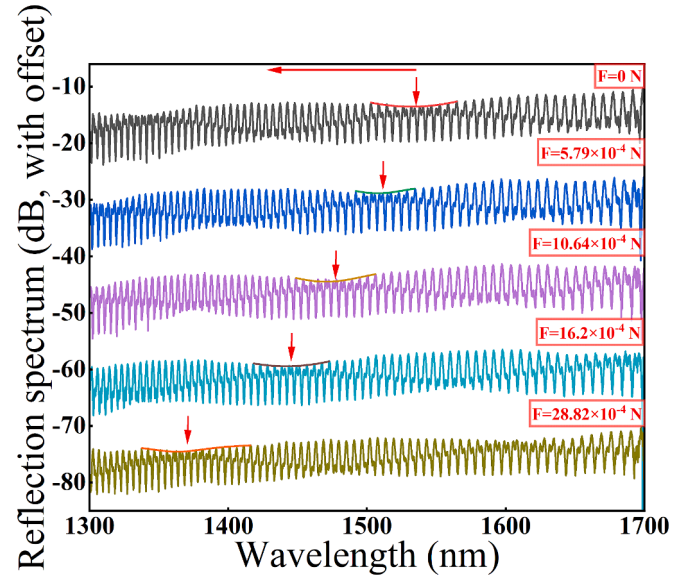


Fig. 3. Partial experimental spectral evolution of Sample 1 as a function of force from 0 to  $28.8 \times 10^{-4} \text{ N}$  (with offset).

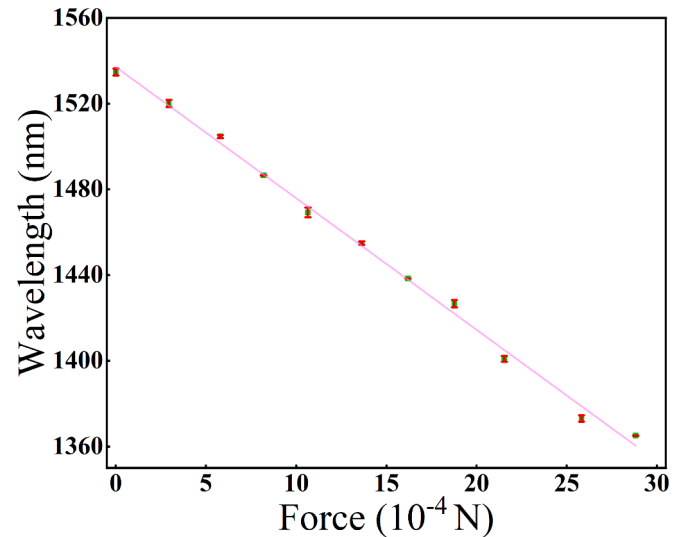


Fig. 4. Linear regression analysis on the experimental results (Sample 1) for the force ranging from 0 to  $28.8 \times 10^{-4} \text{ N}$ .

Cavity<sub>2</sub> is adapted to 3.47 GPa according to upper and lower limit of the composite material [37].

As compared to Cavity<sub>1</sub>, Cavity<sub>2</sub> made of silica features much higher Young's modulus and thus little deformation in response to the applied force. Therefore, Cavity<sub>1</sub> is regarded as a sensing cavity, and Cavity<sub>2</sub> is regarded as a reference cavity. The refractive index of UV adhesive and SMF was set to 1.54 and 1.448, respectively, at room temperature and cross-sectional areas of Cavity<sub>1</sub> and Cavity<sub>2</sub> are set to be  $87844.35 \text{ }\mu\text{m}^2$  (average radius  $\sim 167.26 \text{ }\mu\text{m}$ ) and  $78486.22 \text{ }\mu\text{m}^2$  (average radius  $\sim 158.10 \text{ }\mu\text{m}$ ). The variation of the cavity length is obtained by:

$$\Delta L = \frac{F \times L}{S \times E} \quad (4)$$

where  $F$ ,  $L$ ,  $S$  and  $E$  represent force, initial cavity length, cross-sectional area and Young's modulus, respectively. The simulation results are shown in Fig. 5, suggesting an FSR of  $\sim 230 \text{ nm}$  and a sensitivity of  $-57,688 \text{ nm/N}$  (Figs. 5 and 6), respectively. These results agree well

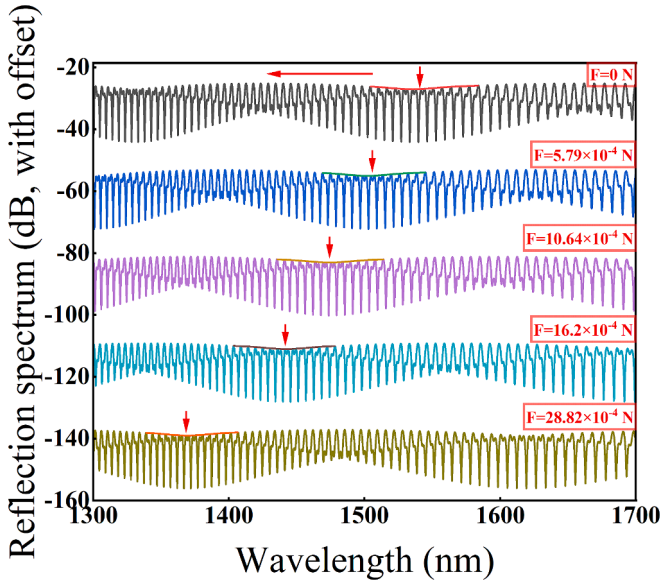


Fig. 5. Simulated spectral evolution of Sample 1 as a function of force 0 to  $28.8 \times 10^{-4}$  N (with offset).

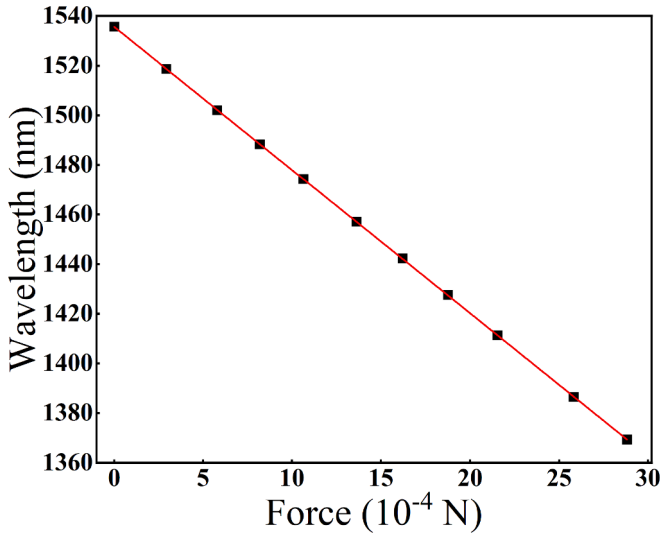


Fig. 6. Linear regression analysis on the simulated results for the force ranging from 0 to  $28.8 \times 10^{-4}$  N.

with the experimental results.

### 3.2. The second sample

For Sample 2,  $L_1$  and  $L_2$  are set to be  $\sim 101 \mu\text{m}$  and  $\sim 109 \mu\text{m}$ , respectively, exhibiting a smaller initial optical path length difference between the sensing and the reference cavity compared to Sample 1. The  $FSR_e$  of the resulting spectrum is  $\sim 500$  nm, which is much larger than that for Sample 1, leading to a more pronounced envelope shift from 1660.8 nm to 1295.3 nm in the force measurement in the range from 0 to  $26.2 \times 10^{-4}$  N, as shown in Fig. 7. This experiment was also conducted for three times, exhibiting good repeatability. The sensitivity of Sample 2 was found to be  $-140,813$  nm/N via the linear fitting, as shown in Fig. 8.

Using the above structural parameters ( $L_1 = 100.96 \mu\text{m}$ ,  $L_2 = 109.10 \mu\text{m}$ ), the simulated spectra are shown in Fig. 9. The cross-sectional areas of UV glue and SMF are set to be  $71,620 \mu\text{m}^2$  (average radius  $\sim 151.03$

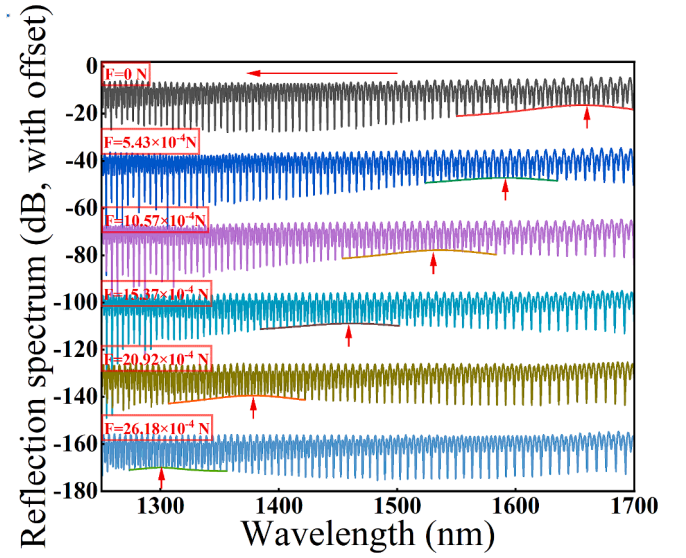


Fig. 7. Partial experimental spectral evolution of Sample 2 as a function of force from 0 to  $26.2 \times 10^{-4}$  N (with offset).

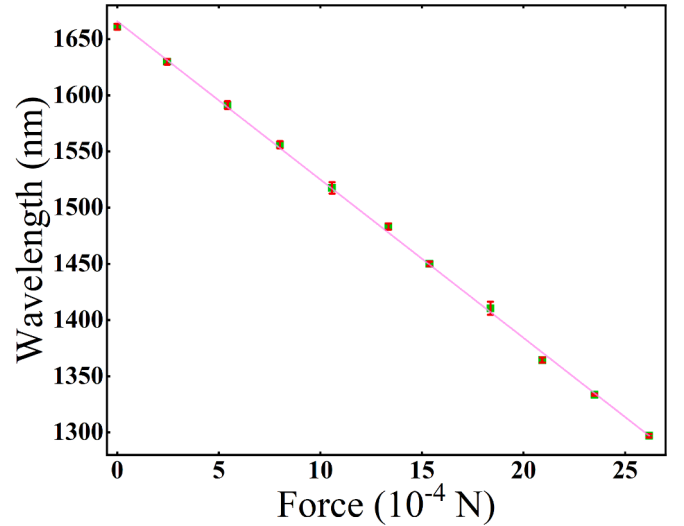


Fig. 8. Linear regression analysis on the experimental results (Sample 2) for the force ranging from 0 to  $26.2 \times 10^{-4}$  N.

$\mu\text{m}$ ) and  $68438.5 \mu\text{m}^2$  (average radius  $\sim 147.63 \mu\text{m}$ ), respectively. The linear fitting of the spectral shift of the envelopes is shown Fig. 10. The corresponding  $FSR_e$  and sensitivity are  $\sim 500$  nm and  $-136453.8$  nm/N, respectively, similar to the experimental results.

We carried out Fast Fourier Transform (FFT) to the experimental spectra of the two samples (Fig. 11). The FFT spectra reflect information with respect to the FSRs of the interference spectra of the individual F-P cavities. For Sample 1 (Fig. 11a), the peak 1 centered at  $\sim 0.164 \text{ nm}^{-1}$  in the spatial frequency domain corresponds to the FSR of the interference spectra of Cavity<sub>1</sub> and Cavity<sub>2</sub>, which is  $\sim 6.10$  nm calculated from Eq. (1). The peak 2 centered at  $\sim 0.332 \text{ nm}^{-1}$  corresponds to the FSR of the spectrum of Cavity<sub>3</sub>, which is  $\sim 3.02$  nm. For Sample 2 (Fig. 11b), the peak 1 and peak 2 centered at  $\sim 0.138 \text{ nm}^{-1}$  and  $\sim 0.279 \text{ nm}^{-1}$ , which corresponds to the FSR of Cavity<sub>1</sub> and Cavity<sub>2</sub> ( $\sim 7.24$  nm) and the FSR of Cavity<sub>3</sub> ( $\sim 3.59$  nm), respectively.

The temperature cross-sensitivity measurement was performed using Sample 2 in the temperature range from  $22^\circ\text{C}$  to  $22.8^\circ\text{C}$  on a temperature-controlled breadboard (Thorlabs, PTC1/M) with a readout resolution of  $\pm 0.001^\circ\text{C}$ . The spectral response of Sample 2 to



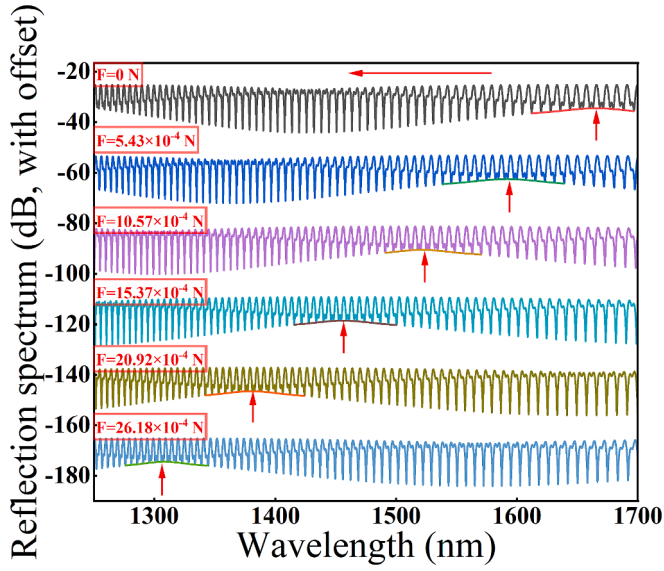


Fig. 9. Simulated spectral evolution of Sample 2 as a function of force from 0 to  $26.2 \times 10^{-4}$  N (with offset).

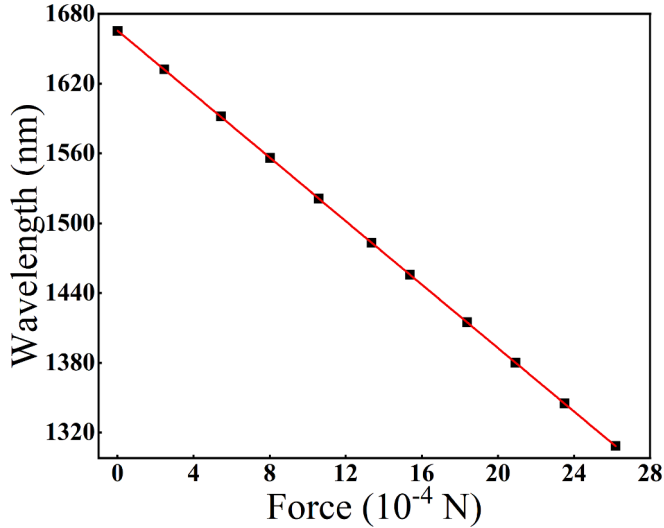


Fig. 10. Linear regression analysis on the simulated results for the force ranging from 0 to  $26.2 \times 10^{-4}$  N.

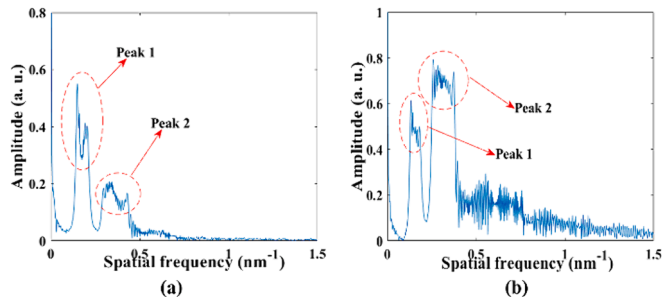


Fig. 11. Spatial frequency spectra obtained by applying FFT to the reflection spectrum of Sample 1 (a) and Sample 2 (b) measured at 0 N.

temperature is shown in the Fig. 12. and the linear fitting of the envelope is depicted in Fig. 13, showing a temperature sensitivity of 413.7 nm/°C. Thus, the application of this sensor probe requires temperature-

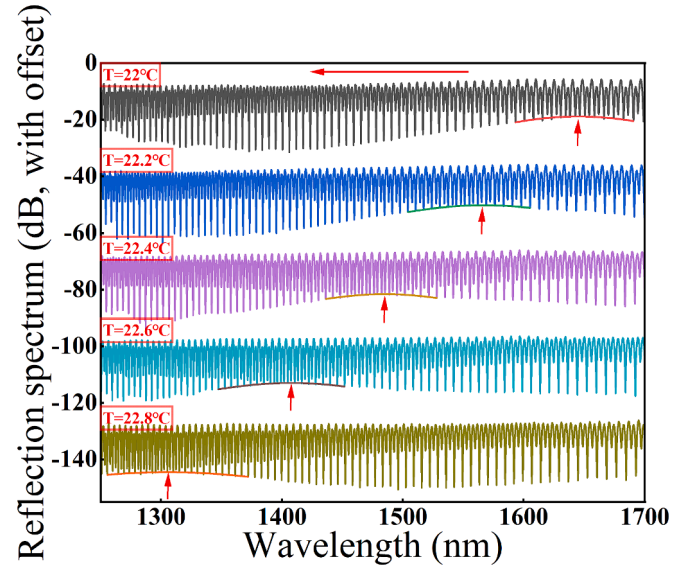


Fig. 12. Partial experimental spectral evolution of Sample 2 as a function of temperature from 22 °C to 22.8 °C (with offset).

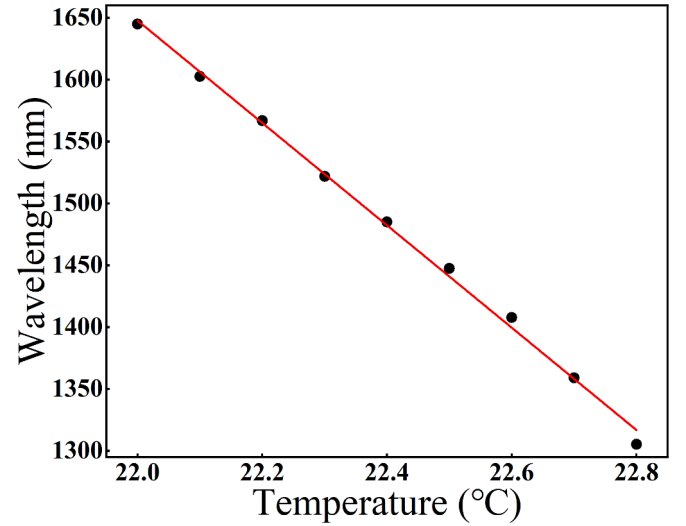


Fig. 13. Linear regression analysis on the experimental results for the temperature ranging from 22 °C to 22.8 °C.

controlled environment. Otherwise, one may need additional temperature sensors to monitor the thermal variations during the force measurements to make compensations. For instance, by fabricating a fiber Bragg grating (FBG) in proposed sensor probe, one could deduce the thermal variations by measuring shifts of the Bragg wavelength, and then compensate the cross sensitivity. However, simultaneous measurement of temperature and force is not the main concern for this paper and will be studied as the future work.

To investigate the sensitivity amplification factor of the Vernier effect, a standard F-P sensor with UV adhesive in the cavity was prepared. The sensor consists of two segments of SMFs with UV adhesive in between. The cavity length is  $\sim 140$   $\mu\text{m}$ . The sensor was annealed in the same condition as previous sensors before force measurement. The obtained spectra are shown in Fig. 14 with a red shift as a function of force in the range of  $0$ – $28.44 \times 10^{-4}$  N. Via linear fitting, a force sensitivity of 1819 nm/N was obtained, as shown in Fig. 15.

Therefore, the sensitivity magnification factor of Sample 2 is about 77.5 ( $140,813/1819 = 77.5$ ), which is on the same scale with the

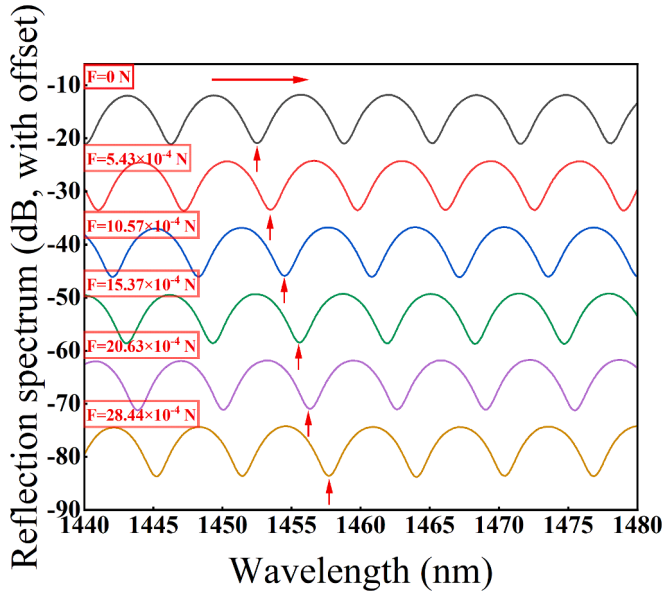


Fig. 14. Partial experimental spectral evolution of F-P as a function of force from 0 to  $28.44 \times 10^{-4}$  N.

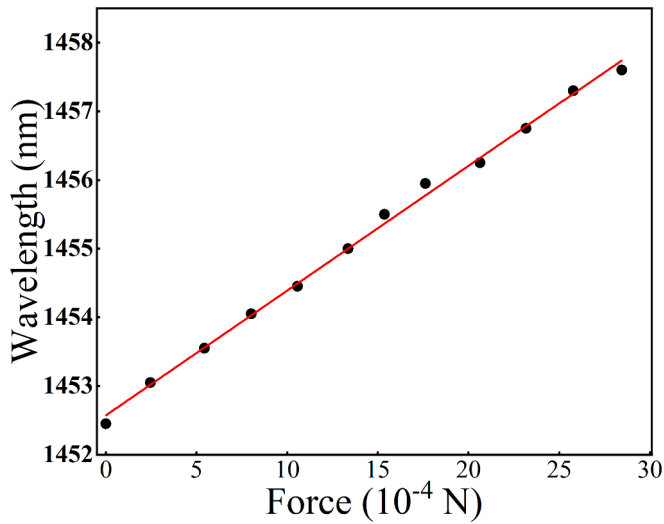


Fig. 15. Linear regression analysis on the experimental results for the force ranging from 0 to  $28.44 \times 10^{-4}$  N.

theoretical calculation value  $\sim 62$  according to the Eq. (3). This higher experimental sensitivity magnification factor could mainly arise from lower force sensitivity of the single F-P sensor due to its larger cavity length ( $\sim 140 \mu\text{m}$ ) compared to  $L_1$  ( $\sim 101 \mu\text{m}$ ) for Sample 2 [16].

Owing to the exceptional sensitivity of Sample 2, it is feasible to measure the evaporation rate of volatile liquids. In this work, the evaporation rate of ethanol was measured, and the spectral evolution of this process is depicted in Fig. 16. We narrowed down the measuring range of the spectrum, focusing only on the small spectral range where the characteristic peaks are located. In this way, we sampled a spectrum every 5 s, while the acquisition time of each spectrum is 1 s. Before carrying out this experiment, a thin glass slide was placed inside the basket. Subsequently, one drop of ( $\sim 3 \mu\text{L}$ ) ethanol were positioned onto the glass slide using a pipette, and an immediate envelope shift was observed from 1452.47 nm to 1444.24 nm. Afterwards, the envelope red-shifted during the ethanol evaporation process. In order to obtain the evaporation rate of ethanol at room temperature, spectra were saved

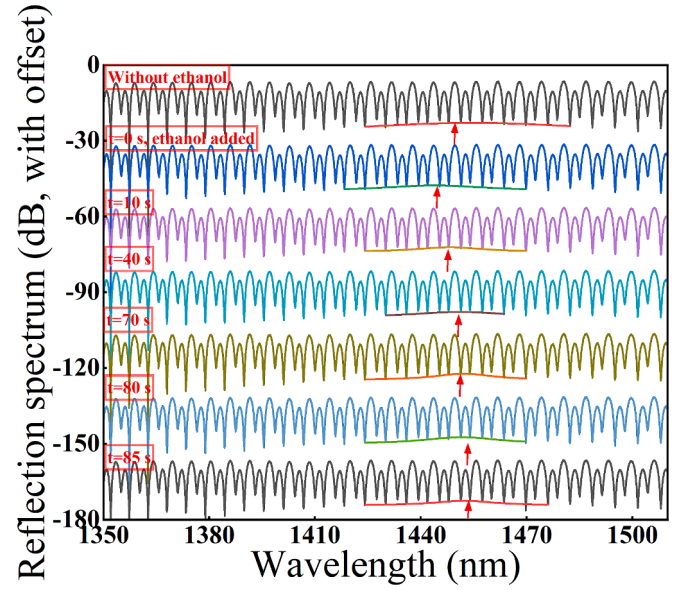


Fig. 16. Partial experimental spectra of ethanol over time (with offset).

every 5 s. This experiment was conducted for three times. According to the force sensitivity of  $-140,813 \text{ nm/N}$  and the evolution of the envelope wavelength as a function of time, the average weight variation of the ethanol is shown in Table 1, and the mass changes of ethanol in 90 s is shown in Fig. 17. In the first 15 s, a evaporation rate of  $7.79 \times 10^{-5} \text{ g/s}$  was obtained after linear fit, and then it decreased gradually until 75 s. This phenomenon could be attributed to the decrease of the surface area of the liquid proportional to the evaporation rate [38]. Note that evaporation rate of a volatile liquid is dependent on many factors such as temperature, pressure, surface area of the liquid. The experiment here aims to demonstrate that the proposed sensor could be used to measure dynamics of changing forces related to physical or biochemical process.

#### 4. Discussions

By comparing the two samples, it is found that the force sensitivity of Sample 2 is much larger than that of Sample 1, which is mainly due to the small optical length difference (OLD) between Cavity<sub>1</sub> and Cavity<sub>2</sub> (the OLD of Sample 1 and Sample 2 are  $\sim 5.1 \mu\text{m}$  and  $\sim 2.5 \mu\text{m}$ , respectively), according to Eqs. (1)–(3). In addition, the sensitivity can be further improved by reducing the OLD between the two cascaded cavities. Theoretically, this sensitivity could actually become much larger, when the OLD diminishes to the infinitesimal (but not 0). However, this also comes with a much larger FSR of the envelope. Subsequently, a single spectral envelope would extend out of the practical measuring range of the spectrum analyzer, leading to an unmeasurable envelope. Thus, a trade-off has to be made between the sensitivity and the practical FSR<sub>e</sub>. Furthermore, the force sensitivity can be improved by reducing the cross-sectional area of the sensing cavity and using a UV adhesive with a much lower Young's modulus. As compared to existing fiber optic force sensors, the proposed sensor features the advantages of

Table 1

The evolution of the envelope wavelength and the weight change of ethanol as function of time due to evaporation.

Times (s)	0	30	60	75	80
Envelope wavelength (nm)	1444.24	1449.62	1451.15	1452.47	1452.47
Ethanol change ( $10^{-3} \text{ g}$ )	0	-3.818	-4.905	-5.840	-5.840

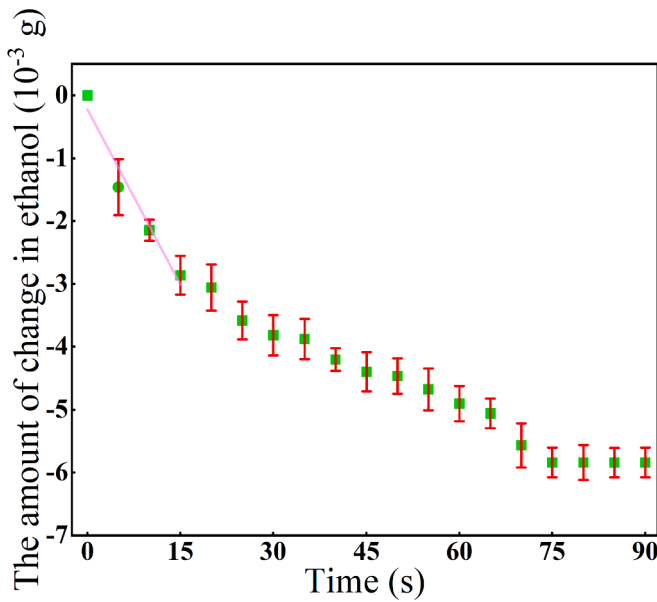


Fig. 17. Changes in mass of ethanol in a 90 s window.

high sensitivity, simple structures and ease of fabrication, as shown in Table 2. For the sensor reported in Refs. [19,20], though the force sensitivity is higher, the fabrication requires fs-laser based high precision 3D printing system, which considerably increases the fabrication cost and complexity of the sensor. In addition, 3D printing is also time-consuming.

What makes our approach even more appealing is that in the fabrication process only standard SMF, capillary fiber and UV adhesive were used. These materials are all commercially available. Besides, there is basically no technical challenges in the sensor fabrication process. Through a simple curing process, a high quality and repeatable force sensor probe could be fabricated.

## 5. Conclusions

In summary, a high-sensitivity force sensor based on the two cascaded F-P cavities and the vernier effect was proposed. Due to the low Young's modulus of the UV glue used to form a cavity, a high force sensitivity is obtained. In both experiment and simulation, we investigated the influence of different optical path lengths on the sensor's sensitivity by using two samples with varying structural parameters. For Sample 1, a sensitivity of  $-64,301$  nm/N was obtained, while for Sample 2, due to reduced OL difference between the two cavities, an even higher sensitivity of  $-140,813$  nm/N was achieved. Repeatability of the sample was also verified. Finally, we used the sensor probe to measure the evaporation rate of ethanol, which was  $7.79 \times 10^{-5}$  g/s at room temperature. Compared to previous sensors, the proposed force sensor is easy to fabricate and cost-effective, and it is an ideal candidate for force measurement.

## CRediT authorship contribution statement

**Hongyu Fu:** Writing – original draft, Software, Methodology, Investigation. **Sisu Peng:** Investigation. **Pengcheng Li:** Writing – review & editing, Supervision, Funding acquisition. **Chuanxin Teng:** Writing – review & editing, Funding acquisition. **Christophe Caucheteur:** Writing – review & editing, Funding acquisition. **Hang Qu:** Writing – review & editing, Supervision, Funding acquisition, Conceptualization. **Xuehao Hu:** Writing – original draft, Supervision, Funding acquisition.

Table 2

Sensitivity comparison of fiber optic force sensor.

Sensitivity (nm/N)	Principle	Fabrication complexity	Force range (μN)	Reference
$1.632 \times 10^1$	Sagnac	Middle	$0-3.92 \times 10^5$	[13]
$2.61 \times 10^1$	F-P	Middle	$0-4.9 \times 10^5$	[14]
$1.1723 \times 10^1$	LPG	Middle	$0-1.11 \times 10^6$	[15]
$4.36 \times 10^8$	F-P, 3D print	High	$0-3.48 \times 10^{-2}$	[19]
$1.54 \times 10^8$	F-P, 3D print	High	$0-6.6 \times 10^{-2}$	[20]
$4.5721 \times 10^7$	F-P, Vernier effect	High	$0-1.4 \times 10^3$	[27]
$3.417 \times 10^1$	FBG	High	$0-1.5 \times 10^7$	[39]
$6.43 \times 10^2$	FBG	Middle	$5 \times 10^3-5 \times 10^4$	[40]
$1.90 \times 10^{-2}$	FBG	High	$0-1 \times 10^7$	[41]
$-1.4047 \times 10^1$	LPFG	Middle	$4.9 \times 10^5-4.508 \times 10^6$	[42]
4.4	SPR, POF	High	$0-5 \times 10^5$	[43]
$1.7527 \times 10^1$	Two-modal interference	Middle	$0-3 \times 10^4$	[44]
$-7.5017 \times 10^{-1}$	F-P	Middle	$0-1.96 \times 10^6$	[45]
$-6.4301 \times 10^4$	F-P, Vernier effect	Low	$0-2.88 \times 10^3$	This work
$-1.40813 \times 10^5$	F-P, Vernier effect	Low	$0-2.62 \times 10^3$	This work

## Declaration of competing interest

The authors declare that they have no known competing financial interests or personal relationships that could have appeared to influence the work reported in this paper.

## Data availability

Data will be made available on request.

## Acknowledgment

This work was supported by Science and Technology Department of Guangdong Province (No. 2022A1515012571); Natural Science Foundation of Guangxi Province (2023GXNSFDA026040); National Natural Science Foundation of China (12074239); Shantou University (NTF22026, NTF23011); The Fonds de la Recherche Scientifique (F.R.S.-FNRS) under the Postdoctoral Researcher grant (Chargé de Recherches) of Xuehao Hu and the Senior Research Associate Position of Christophe Caucheteur. The associate editor coordinating the review of this article and approving it for publication was XXXX. (Corresponding author: Hang Qu, Xuehao Hu)

## References

- [1] W. Yang, W. Li, H. Lu, J. Liu, T. Zhang, Dynamic compensation method for humidity sensors based on temperature and humidity decoupling, *Sensors (Basel)* 22 (19) (2022) 7229.
- [2] S. Liu, Y. Ji, J. Yang, W. Sun, H. Li, Nafion film temperature/humidity sensing based on optical fiber Fabry-Perot interference, *Sens. Actuators, A* 269 (2018) 313–321.
- [3] Z. Li, W. Dang, J. Dan, K. Jin, P. Nan, G. Xin, K.-S. Lim, H. Ahmad, H. Yang, High-sensitivity interferometric high-temperature strain sensor based on optical harmonic Vernier effect, *Opt. Fiber Technol.* 79 (2023) 103361.
- [4] Y.-J. Ee, Z. Kufian, K.-S. Lim, K.-S. Tey, C.-W. Ooi, W. Udos, Z. Osman, H. Ahmad, Highly sensitive Vernier sensor based on chirp grating Fabry-Perot interferometer (CG-FPI) for the strain detection in lithium polymer (LiPo) batteries, *Sens. Actuators, A* 350 (1) (2023) 114080.
- [5] Q. Wang, W. Zhao, B. Wang, H. Hu, J. Li, A high sensitivity refractive index sensor based on photonic crystal fibre Mach-Zehnder interferometer, *J. Mod. Opt.* 64 (16) (2017) 1639–1647.
- [6] F. Ahmed, V. Ahsani, S. Jo, C. Bradley, E. Toyserkani, M.B.G. Jun, Measurement of in-fiber refractive index change using a Mach-Zehnder interferometer, *IEEE Photon. Technol. Lett.* 31 (1) (2019) 74–77.

- [7] H. Huang, X. Zhu, C. Jiang, H. Chen, J. Song, Y. Wang, S. Sun, High sensitivity temperature sensor based on enhanced Vernier effect through two parallel Fabry-Perot cavities, *Appl. Opt.* 62 (2) (2023) 275–283.
- [8] B. Huang, X. Sheng, Z. Tang, X. Wang, S. Lou, High and online tunable sensitivity fiber temperature sensor based on Vernier-effect, *Opt. Fiber Technol.* 72 (2022) 103003.
- [9] J. Zhang, C. Wang, Y. Chen, Y. Xiang, T. Huang, P.P. Shum, Z. Wu, Fiber structures and material science in optical fiber magnetic field sensors, *Front Optoelectron* 15 (1) (2022) 34.
- [10] X.-X. Wang, Y. Zhao, R.-Q. Lv, H.-K. Zheng, Optic-fiber vector magnetic field sensor utilizing magneto-shape effect of magnetic fluid, *Measurement* 202 (2022) 111829.
- [11] D. Xiao, G. Wang, F. Yu, S. Liu, W. Xu, L. Shao, C. Wang, H. Fu, S. Fu, P.P. Shum, T. Ye, Z. Song, W. Wang, Optical curvature sensor with high resolution based on in-line fiber Mach-Zehnder interferometer and microwave photonic filter, *Opt. Express* 30 (4) (2022) 5402–5413.
- [12] H. Gong, H. Song, X. Li, J. Wang, X. Dong, An optical fiber curvature sensor based on photonic crystal fiber modal interferometer, *Sens. Actuators, A* 195 (1) (2013) 139–141.
- [13] Q. Liu, L. Xing, Z. Wu, L. Cai, Z. Zhang, J. Zhao, High-sensitivity photonic crystal fiber force sensor based on Sagnac interferometer for weighing, *Opt. Laser Technol.* 123 (2020) 105939.
- [14] Y. Liu, S. Qu, W. Qu, R. Que, A Fabry-Perot cuboid cavity across the fibre for high-sensitivity strain force sensing, *J. Opt.* 16 (10) (2014) 105401.
- [15] F.O. Barino, R. Luiz Faraco-Filho, D. Campos, A. Bessa dos Santos, 3d-printed force sensitive structure using embedded long-period fiber grating, *Opt. Laser Technol.* 148 (2022) 107697.
- [16] G. Wei, Q. Jiang, T. Zhang, A flexible force sensor based on spheroidal Fabry-Perot micro-cavity, *Optik* 181 (2019) 483–492.
- [17] Arata, Nitta, Nakatsuka, Kawabata, Matsunaga, Haga, Harada, Mitsuishi, Modular optic force sensor for a surgical device using a Fabry-Perot interferometer, *Appl. Sci.* 9 (17) (2019) 3454.
- [18] Y. Liu, C. Lang, X. Wei, S. Qu, Strain force sensor with ultra-high sensitivity based on fiber inline Fabry-Perot micro-cavity plugged by cantilever taper, *Opt. Express* 25 (7) (2017) 7797–7806.
- [19] X.-G. Shang, N. Wang, S.-M. Cao, H.-H. Chen, D.-X. Fan, N.-J. Zhou, M. Qiu, Fiber-integrated force sensor using 3d printed spring-composed Fabry-Perot cavities with a high precision down to tens of piconewton, *Adv. Mater.* 36 (2) (2023) 2305121.
- [20] F.-M. Wang, M.-Q. Zou, C.-R. Liao, B.-Z. Li, D.-J. Liu, J. Zhou, H.-Q. Huang, J.-L. Zhao, C. Liu, P.-K. Chu, Y.-P. Wang, Three-dimensional printed microcantilever with mechanical metamaterial for fiber-optic microforce sensing, *APL Photonics* 8 (9) (2023) 096108.
- [21] P. Zhang, M. Tang, F. Gao, B. Zhu, Z. Zhao, L. Duan, S. Fu, J. Ouyang, H. Wei, P. P. Shum, D. Liu, Simplified hollow-core fiber-based Fabry-Perot interferometer with modified Vernier effect for highly sensitive high-temperature measurement, *IEEE Photonics J.* 7 (1) (2015) 1–10.
- [22] Y. Chen, L. Zhao, S. Hao, J. Tang, Advanced fiber sensors based on the Vernier effect, *Sensors (Basel)* 22 (7) (2022) 2694.
- [23] A.D. Gomes, H. Bartelt, O. Frazão, Optical Vernier effect: recent advances and developments, *Laser Photonics Rev.* 15 (7) (2021) 2000588.
- [24] K.-Y. Wu, O'Malley, N. P. Fatema, C. Wang, M. Girardi, M. S. Alshaykh, Z.-C. Ye, D. E. Leaird, M.-H. Qi, A. M. Weiner, Verner Microcombs for Integrated Optical Atomic Clocks, *arXiv preprint arXiv:2308.08937*.
- [25] Y. Liu, X. Li, Y.-N. Zhang, Y. Zhao, Fiber-optic sensors based on Vernier effect, *Measurement* 167 (1) (2021) 108451.
- [26] X. Zhao, Y. Zhang, W. Zhang, Z. Li, Y. Yue, T. Yan, Ultrasensitive Fabry-Perot strain sensor based on Vernier effect and tapered FBG-in-hollow silica tube, *IEEE Sens. J.* 21 (3) (2021) 3035–3041.
- [27] W. Bao, X. Li, F. Chen, R. Wang, X. Qiao, Hyperelastic polymer fiber fabry-pérot interferometer for nanoforce measurement, *J. Lightwave Technol.* 40 (12) (2022) 4020–4026.
- [28] R. Oliveira, L. Bilro, R. Nogueira, A.M. Rocha, Adhesive based Fabry-Perot hydrostatic pressure sensor with improved and controlled sensitivity, *J. Lightw. Technol.* 37 (9) (2019) 1909–1915.
- [29] C.-L. Lee, R.-C. Zeng, C.-R. Yang, C.-F. Lin, C.-T. Ma, W.-F. Liu, Tapered polymer fiber inclinometers, *IEEE Photonics J.* 12 (3) (2020) 7100910.
- [30] G. Salceda-Delgado, A. Van Newkirk, J.E. Antonio-Lopez, A. Martinez-Rios, A. Schulzgen, R. Amezcua-Correa, Optical capillary fiber mode interferometer for pressure sensing, *IEEE Sens. J.* 20 (5) (2020) 2253–2260.
- [31] H. Qiu, J. Jiang, L. Yao, Z. Dai, Z. Liu, H. Qu, X. Hu, Ultrasensitive cascaded in-line Fabry-Perot refractometers based on a C-shaped fiber and the Vernier effect, *Opt. Express* 30 (15) (2022) 27704–27714.
- [32] A.D. Gomes, M.S. Ferreira, J. Bierlich, J. Kobelke, M. Rothhardt, H. Bartelt, O. Frazao, Optical harmonic Vernier effect: a new tool for high performance interferometric fibre sensors, *Sensors (Basel)* 19 (24) (2019) 5431.
- [33] Y. Li, C. Zhao, B. Xu, D. Wang, M. Yang, Optical cascaded Fabry-Perot interferometer hydrogen sensor based on Vernier effect, *Opt. Commun.* 414 (2018) 166–171.
- [34] J. Zhang, H. Liao, P. Lu, X. Jiang, X. Fu, W. Ni, D. Liu, J. Zhang, Ultrasensitive temperature sensor with cascaded fiber optic Fabry-Perot interferometers based on Vernier effect, *IEEE Photonics J.* 10 (5) (2018) 1–11.
- [35] Norland Optical Adhesive 73, Available online: <https://www.norlandprod.com/adhesives/noa%2073.html>.
- [36] P. Antunes, F. Domingues, M. Granada, P. André, Mechanical properties of optical fibers, *INTECH Open Access Publisher*, 2012.
- [37] H.X. Zhu, T.X. Fan, D. Zhang, Composite materials with enhanced dimensionless Young's modulus and desired Poisson's ratio, *Sci. Rep.* 5 (2015) 14103.
- [38] O. Carrier, N. Shahidzadeh-Bonn, R. Zargar, M. Aytouna, M. Habibi, J. Eggers, D. Bonn, Evaporation of water: evaporation rate and collective effects, *J. Fluid Mech.* 798 (2016) 774–786.
- [39] A.G. Leal-Junior, A. Theodosiou, C. Marques, M.J. Pontes, K. Kalli, A. Frizera, Thermal treatments and compensation techniques for the improved response of FBG sensors in POFs, *J. Lightwave Technol.* 36 (17) (2018) 3611–3617.
- [40] G. Rajan, B. Liu, Y. Luo, E. Ambikairajah, G.-D. Peng, High sensitivity force and pressure measurements using etched singlemode polymer fiber bragg gratings, *IEEE Sens. J.* 13 (5) (2013) 1794–1800.
- [41] P. Di Palma, E. De Vita, A. Iadicco, S. Campopiano, Force sensor based on FBG embedded in silicone rubber, *IEEE Sens. J.* 23 (2) (2023) 1172–1178.
- [42] W. Luo, Y. Wang, Q. Ling, Z. Guan, D. Chen, Q. Wu, An axial force sensor based on a long-period fiber grating with dual-peak resonance, *Photonics* 10 (5) (2023) 591.
- [43] F. Arcadio, L. Zenl, N. Cennamo, Exploiting plasmonic phenomena in polymer optical fibers to realize a force sensor, *Sensors (Basel)* 22 (6) (2022) 2391.
- [44] J. Zhao, D. Jia, A. Nie, H. Zhang, T. Liu, Compact vectorial transverse force sensor based on two-modal interference in a few-mode seven-core fiber, *J. Lightwave Technol.* 38 (7) (2020) 2046–2052.
- [45] Y. Zhao, F. Xia, M.-Q. Chen, R.-J. Tong, Y. Peng, Optical fiber axial contact force sensor based on bubble-expanded Fabry-Pérot interferometer, *Sens. Actuators, A* 272 (2018) 318–324.